NeuroImage 248 (2022) 118868

Contents lists available at ScienceDirect

NeuroImage

journal homepage: www.elsevier.com/locate/neuroimage

Comparing BOLD and VASO-CBV population receptive field estimates in human visual cortex

Ícaro A.F. Oliveira[a,b,*], Yuxuan Cai[a,b], Shir Hofstetter[a], Jeroen C.W. Siero[a,d], Wietske van der Zwaag[a], Serge O. Dumoulin[a,b,c]

[a] Spinoza Centre for Neuroimaging, Meibergdreef 75, Amsterdam 1105 BK, the Netherland
[b] Experimental and Applied Psychology, VU University, Amsterdam, the Netherland
[c] Experimental Psychology, Helmholtz Institute, Utrecht University, Utrecht, the Netherland
[d] Radiology, Utrecht Center for Image Sciences, University Medical Center Utrecht, Utrecht, the Netherland

ARTICLE INFO

Keywords:
Vascular space occupancy
VASO
Cerebral blood volume
BOLD
Visual cortex
pRF
Vascular contribution

ABSTRACT

Vascular Space Occupancy (VASO) is an alternative fMRI approach based on changes in Cerebral Blood Volume (CBV). VASO-CBV fMRI can provide higher spatial specificity than the blood oxygenation level-dependent (BOLD) method because the CBV response is thought to be limited to smaller vessels. To investigate how this technique compares to BOLD fMRI for cognitive neuroscience applications, we compared population receptive field (pRF) mapping estimates between BOLD and VASO-CBV. We hypothesized that VASO-CBV would elicit distinct pRF properties compared to BOLD. Specifically, since pRF size estimates also depend on vascular sources, we hypothesized that reduced vascular blurring might yield narrower pRFs for VASO-CBV measurements. We used a VASO sequence with a double readout 3D EPI sequence at 7T to simultaneously measure VASO-CBV and BOLD responses in the visual cortex while participants viewed conventional pRF mapping stimuli. Both VASO-CBV and BOLD images show similar eccentricity and polar angle maps across all participants. Compared to BOLD-based measurements, VASO-CBV yielded lower tSNR and variance explained. The pRF size changed with eccentricity similarly for VASO-CBV and BOLD, and the pRF size estimates were similar for VASO-CBV and BOLD, even when we equate variance explained between VASO-CBV and BOLD. This result suggests that the vascular component of the pRF size is not dominating in either VASO-CBV or BOLD.

1. Introduction

The majority of functional MRI (fMRI) studies employ blood oxygenation level-dependent (BOLD) contrast (Glover, 2011; Ogawa et al., 1990). BOLD contrast reflects a combination of changes in venous blood oxygenation, cerebral blood flow (CBF), and cerebral blood volume (CBV) (Buxton et al., 2014). The Gradient Echo (GE) BOLD sequence is the typical method of choice, mainly because of its superior sensitivity, available Signal-to-Noise Ratio (SNR), and high coverage (Havlicek and Uludağ, 2020). Unfortunately, this sequence suffers from limited spatial specificity due to contamination of the functional signal with draining and pial veins effect (Kim and Ogawa, 2012; Menon, 2002; Uludağ et al., 2009).

Vascular Space Occupancy (VASO) is a non-invasive fMRI technique sensitive to changes in CBV (Lu et al., 2013, 2003). The VASO sequence and its variants take advantage of the T1 differences between arterial blood and the surrounding tissue to null the blood signal and measure CBV changes (Lu et al., 2003). An inversion recovery pulse is used to minimize blood signal while a substantial part of the tissue signal remains available for detection. The increased cerebral blood volume results in a negative signal change during the neuronal activity, caused by the tissue signal reduction in the voxel. VASO-CBV contrast promises higher microvascular specificity since it is sensitive to arteriole and post-arterial CBV changes, resulting in better spatial localization of the neuronal activity with reduced draining vein contamination than BOLD (Huber et al., 2014; Jin and Kim, 2008).

The VASO-CBV sequence variant developed by Huber et al. (2014) for 7T scanners has proven to be a highly effective alternative for high-resolution acquisitions, especially for

Abbreviations: fMRI, functional magnetic resonance imaging; BOLD, blood oxygenation level-dependent; CBV, cerebral blood volume; VASO, vascular space occupancy; CBF, cerebral blood flow; GE, Gradient Echo; pRF, population receptive field; HRF, hemodynamic response function; EPI, echo planar imaging; ROI, region of interest; AAT, arterial arrival time; GM, grey matter; WM, white matter; TI, inversion time; TE, echo time; FA, flip angle; SNR, signal-to-noise ratio.

* Corresponding author at: Spinoza Centre for Neuroimaging, Meibergdreef 75, Amsterdam 1105 BK, the Netherland.
E-mail address: i.oliveira@spinozacentre.nl (Í.A.F. Oliveira).

https://doi.org/10.1016/j.neuroimage.2021.118868.
Received 28 October 2021; Received in revised form 20 December 2021; Accepted 29 December 2021
Available online 30 December 2021.

depth-dependent applications (Beckett et al., 2020; Huber et al., 2020b, 2017, 2015; Persichetti et al., 2019; Yu et al., 2019). Another remark of the 7T VASO fMRI is that the sequence was recently validated against established preclinical imaging modalities (Huber et al., 2021). In addition, significant improvements in accelerated acquisition techniques, such as 3D EPI readout (Huber et al., 2018a) and increased spatial coverage with MAGEC VASO (Huber et al., 2020a), enabled the possibility of a broader number of applications. Multiple studies have demonstrated the feasibility of using VASO fMRI for advanced neuroimaging applications (Finn et al., 2019; Huber et al., 2020b; Lu et al., 2005). However, to date, VASO-CBV responses have not been extended to more complex paradigms and computational models, such as population receptive field mapping.

Here, we evaluate the feasibility of VASO-CBV in the visual cortex using population receptive field (pRF) modeling (Dumoulin and Wandell, 2008). The pRF is the region of visual space that elicits a response for a given cortical location (Victor et al., 1994). The pRF analysis with fMRI has become a popular method to study the topographic organization of primary sensory neural populations and has been extended to several perceptual, cognitive, and clinical domains (Dumoulin and Knapen, 2018; Wandell and Winawer, 2015). The conventional pRF model characterizes the pRF with a two-dimensional Gaussian function with three parameters: position (x,y or eccentricity, and polar angle) and size (sigma). Both neural and non-neural components contribute to the pRF size (Dumoulin and Wandell, 2008). Neural components include both single-neuron receptive field size and positional scatter. Non-neural components include methodological aspects of head and eye movements, but also vasculature, such as hemodynamic response function (HRF) and vascular point spread function (Dumoulin and Wandell, 2008; Lerma-Usabiaga et al., 2020). Since pRF properties have both vascular and neuronal contributions and the vascular contributions to pRF size are expected to be smaller in VASO-CBV, we hypothesized that the VASO-CBV responses are more specific than BOLD responses.

Thus the present work extends the use of the VASO-CBV technique to the population receptive field modeling. The aim is to evaluate and compare VASO-CBV and BOLD pRF estimates such as eccentricity and polar angle maps in addition to the pRF size, using a standard pRF mapping approach in the visual cortex. We first used a dartboard flickering checkerboard stimuli to determine the optimal slice orientation for VASO-fMRI in the visual cortex. With the optimized slice orientation, we measured pRF estimates in visual field maps V1–V3 simultaneously using a double readout 3D-EPI VASO sequence to test the hypothesis that the higher spatial specificity of VASO-CBV would translate to smaller pRF size estimates.

2. Materials and methods

2.1. Participants

The measurements were obtained from six healthy participants (five females, age 32 ± 7 years [Mean ± SD]). Three participants participated in the slice orientation experiment (P01–P03). The other three volunteers participated in the pRF experiment (P04–P06). All participants had normal or corrected-to-normal visual acuity. The ethics committee of the Amsterdam University Medical center - location AMC approved this study, and all volunteers provided written consent before participating after being informed of the experimental procedures.

2.2. Visual stimuli setup

Visual stimuli were presented on a 69.84 × 39.29 cm LCD screen (Cambridge Research System) placed at the end of the scanner's bore. Participants viewed the display through a mirror mounted on top of the coil. The distance from the mirror to the display screen was 220 cm, and the display resolution was 1920 × 1080 pixels. The visual stimuli were generated in Matlab (The MathWorks, Natick, United States) using PsychToolbox Version 3 (Brainard, 1997; Kleiner et al., 2007).

2.2.1. Slice orientation experiment

We determined the optimal slice orientation for VASO fMRI in the visual cortex using a dartboard-shaped flickering checkerboard stimulus. The dartboard was subdivided into 13 rings and 24 segments, totalizing 312 sectors. These sectors changed their contrast between 2 levels of luminance (black and white) in a frequency rate of 2 Hz. Each experiment run consisted of 24 s of stimulation followed by 24 s of baseline, with an extra 12 s of fixation at the start of each run.

2.2.2. pRF experiment

The pRF mapping paradigm was similar to that described in previous studies (Dumoulin and Wandell, 2008; Harvey and Dumoulin, 2011). The stimulus consisted of bar apertures with a moving checkerboard pattern (100% contrast) that moved across the visual field. The width of the bar subtended 1/4th of the stimulus radius (1.25°). Four bar orientations (0°, 45°, 90°, and 135°) and two different motion directions for each bar were used, giving a total of 8 different bar configurations within a given scan. The bar sweeps across the stimulus aperture in 12 TRs (when the bar orientation is 45° and 135°) followed by a mean luminance period of 4 TRs, or in 16 TRs (when the bar orientation is 0° and 90°) with no blank period. Diagonally and orthogonally oriented sweeps were interleaved during each scan.

Participants were asked to fixate on the dot (0.125 radius) in the center of the visual stimulus and press a button every time the dot color changed. The dot changed between red and green at random intervals to ensure the participant's attention to the presented stimulus. Each participant's measurement was repeated twice in two separate sessions with seven runs to obtain higher temporal SNR.

2.3. MR sequences

A Slice-selective Slab-Inversion (SS-SI) VASO with a double 3D readout (Huber et al., 2018a, 2014; Oliveira et al., 2021b) was implemented on a 7T MRI scanner (Philips Healthcare, Best, The Netherlands). All data were acquired using an 8 channel transmit coil and a 32 channel receive coil (Nova Medical Inc, Wilmington, United States). We used a global B1 shim set from a previously assessed group of volunteers to achieve a, close to, circular polarization (quadrature) transmission mode (Oliveira et al., 2021a).

The visual cortex has a longer arterial arrival time (AAT) than other brain areas (Mildner et al., 2014). However, contamination by the inflow of non-inverted blood can be minimized if the blood T1 is much shorter than the TR (Donahue et al., 2009; Huber et al., 2018b). To minimize the inflow effect, the inversion time was kept relatively short. The timing parameters for the interleaved acquisition are $TI_1/TI_2/TE/TR$ = 1100/2600/15/3000 ms. In addition, an adiabatic inversion TR-FOCI pulse was used to ensure an effective inversion with reduced B1+ inhomogeneity (Hurley et al., 2010). The voxel size used in the present study is close to the resolution typically used in pRF modeling (Aqil et al., 2021; Cai et al., 2021b; Hofstetter et al., 2021). Data were acquired with an isotropic voxel size of 1.75 mm, FOV = 196 × 196 × 32 mm^3, matrix size = 112 × 112, 18 slices, partial Fourier factor = 0.78 in the phase encoding direction and $SENSE_{inplane}$ factor = 2.5 with constant flip angle, flip angle (FA) = 15°. We included a fat suppression module Spectral Attenuated Inversion Recovery (SPAIR) before VASO-CBV and BOLD readout blocks with the same settings (TI = 360 ms, TR = 754 ms, pulse duration ~ 20 ms). The vendor's specific absorption ratio (SAR) values never exceeded 65% of the local SAR limit. Both experiments used the same SS-SI-VASO sequence. For the slice orientation experiment, 100 vol were acquired per 5 min run, with 1 run for each orientation, and run order varied between participants. For the pRF experiment, 132 vol were acquired per run, leading to a total scan time of 6 min and 42 s.

Anatomical scans were acquired in separate sessions with the MP2RAGE sequence (Marques et al., 2010; Oliveira et al., 2021a) at the isotropic resolution of 0.64 mm, $TR_{MP2RAGE}$= 5500 ms, TR/TE = 6.2/2.2 ms, TI_1/TI_2 = 800/2700 ms with FA = 7°/5°. For one of the participants, a previously acquired dataset was used as an anatomical reference (0.8 mm).

We optimized the VASO-CBV scanning protocol for the visual cortex. Four different orientations of the slab, together with a change in the direction of the readout gradient orientation, were compared. Note that the slab positioning influences the amount of inflow, the amount of available tissue signal in VASO measurements and SENSE unfolding performance. The slice orientations (Fig. 1) were defined as follows: (I) Aligned with the ACPC-axis (Anterior-Posterior Commissure) covering the calcarine sulcus obliquely, with the phase encoding in the Anterior-Posterior direction. (II) Aligned with the calcarine sulcus with phase encoding in the Anterior-Posterior direction. (III) Aligned with the superior surface of the cerebellum, covering the calcarine sulcus (coronal orientation), with phase encoding in the Right-Left direction. (IV) Purely coronal slices, again with phase encoding in the Right-Left direction.

2.4. Data analysis

2.4.1. Slice orientation experiment

Raw images were corrected for head-motion, with a separate realignment for VASO and BOLD in SPM12 (Statistical Parametric Mapping) software package using default settings, followed by a BOLD correction to account for the $T2^*$ dependency in the VASO images (Huber et al., 2014). The optimal slice orientation for VASO fMRI in the visual cortex was determined by the highest level of activation represented by the highest average Z-scores obtained from FEAT (FSL, v.6.0). The region of interest (ROI) definition consisted of the shared VASO-CBV activated voxels within gray matter in all orientations with a minimum Z-score of 1.5, which we will dub as overlap ROI. The Z-score differences were assessed using a one-way repeated measures ANOVA with post-hoc Holm correction. In addition, we also evaluated the Temporal Signal-to-Noise Ratio (tSNR) using two cubic ROIs (12 × 12 × 12 mm) in the visual cortex. The tSNR differences were also assessed using one-way repeated ANOVA with the same post-hoc analysis.

2.4.2. pRF experiment

T1w images were segmented into gray and white matter using cbstools (Bazin et al., 2014) and resampled to a 1 mm isotropic resolution. The pre-processing steps were the same as in the slice orientation experiment. No additional spatial smoothing or temporal filtering was applied to minimize the loss in specificity.

Pre-processed functional data were then analyzed in the vistasoft software (https://github.com/vistalab/vistasoft). The first four volumes of the functional data were discarded to ensure steady-state magnetization. The first VASO-CBV volume was aligned to the segmented anatomy, resulting in a 4 × 4 transform matrix in each session. Individual functional images in the session were co-registered to the same anatomical space using the same transformation. VASO-CBV and BOLD functional data were averaged across runs, respectively. Since the VASO-CBV mechanism generates a negative intensity response, all VASO-CBV time series were flipped by removing the mean, inverting the signal polarity, and adding the mean.

We estimated the population receptive field position and sizes using the conventional Gaussian pRF model (Dumoulin and Wandell, 2008). First, the functional response of each voxel is predicted using a two-dimensional Gaussian pRF model. The predicted fMRI time course is calculated by the convolution of the modeled pRF, the stimulus sequence, and a canonical BOLD HRF (Boynton et al., 1996; Friston et al., 1998). The quantitative pRF parameters for each voxel are determined by minimizing the residual sum of squared errors (RSS) between the predicted and the observed fMRI time series. After estimating these pRF parameters, we estimated the HRF parameters by minimizing the RSS between the predicted and the observed responses over the visual cortex, where the pRF model explained > 10% of the variance in the data. We used the new HRF to refine the pRF estimates (Harvey and Dumoulin, 2011). We analyzed the data both with and without the final HRF fit stage. The results were similar (Supplementary Fig. 1).

We included voxels for further analysis based on two criteria. First, we only used voxels in V1–V3. Second, we limited the analysis to those voxels where the R^2 corresponded to a p-value less than 0.05 in the VASO data. The variance explained (R^2) was converted to p-values using the same principle as shown in Hofstetter and Dumoulin (2021). We created a null distribution using the same model-fitting procedure on voxels taken from the white matter (WM) pooled across participants (P04: 44,912 voxels; P05: 40,920 voxels, and P06: 67,890 voxels). For each variance explained, the proportion of these voxels with model fits were calculated. The variance explained of the pRF model was 21%, resulting in an equivalent probability of 0.048 of observing this goodness of fit by chance. Note that using these criteria, we are not excluding the possibility of including voxels in the ROI that have below-threshold variance explained in the BOLD data. For P04, this is the case in less than 1% of the voxels in each ROI (V1–V3). For P05, in V1, and V3, less than 1% of the voxels had lower than 21% of variance explained, and 2% in V2. For P06, all voxels had higher than 21% of the variance explained in BOLD data.

Next, population receptive field sizes were estimated as a function of eccentricity for V1–V3. We used unbinned data to estimate the best linear relationship (slope and offset) and used data between 0.5 and 4.5 visual degrees to avoid pRFs close to the fovea and to account for the boundaries of the stimulus display. The data was binned for visualization purposes only. To assess BOLD and VASO–CBV pRF size differences, the pRF size from the central eccentricity was calculated using the slope and intercept values per participant and per ROI (V1–3). The comparison was performed between each BOLD run separately against the averaged VASO (14 runs) to approximate the variance explained. A one-way Bayesian ANOVA using JASP software was used to assess the statistical differences (JASP team, 2021). The Pearson's correlation and the plots were generated in R Core Team (2020).

2.5. Noise level assessment

The noise level was evaluated using two metrics: tSNR and variance explained (Cai et al., 2021a). For both metrics, the quantification was calculated as a function of the number of runs. The tSNR was separately estimated for the BOLD and VASO time series after motion correction and co-registration between both sessions. Gray and white matter masks were defined as the intersection of the relevant output of the segmentation of the anatomical data with the functional slab. The tSNR was calculated cumulatively across runs, the BOLD and VASO tSNR was calculated as the mean value across gray matter (GM) and white matter (WM) divided by the standard deviation across the same regions. The order of the runs was randomized within ten iterations. The variance explained was estimated per voxel by computing the variance after fitting the BOLD and VASO-CBV time series separately with the model prediction of a given voxel. The voxel's prediction of a single BOLD run was used as the model prediction for BOLD and VASO-CBV datasets. For the variance explained assessment, only voxels in V1 were used. The order of the runs was also randomized within ten iterations.

3. Results

3.1. Optimal slice orientation for VASO-CBV

We evaluated four different slice orientations to find the optimal orientation for visual responses in a VASO-CBV experiment: (I) Aligned with the Anterior-Posterior Commissure covering the calcarine sulcus with the phase encoding in the Anterior-Posterior direction, (II) parallel to the calcarine sulcus with phase encoding in the Anterior-Posterior

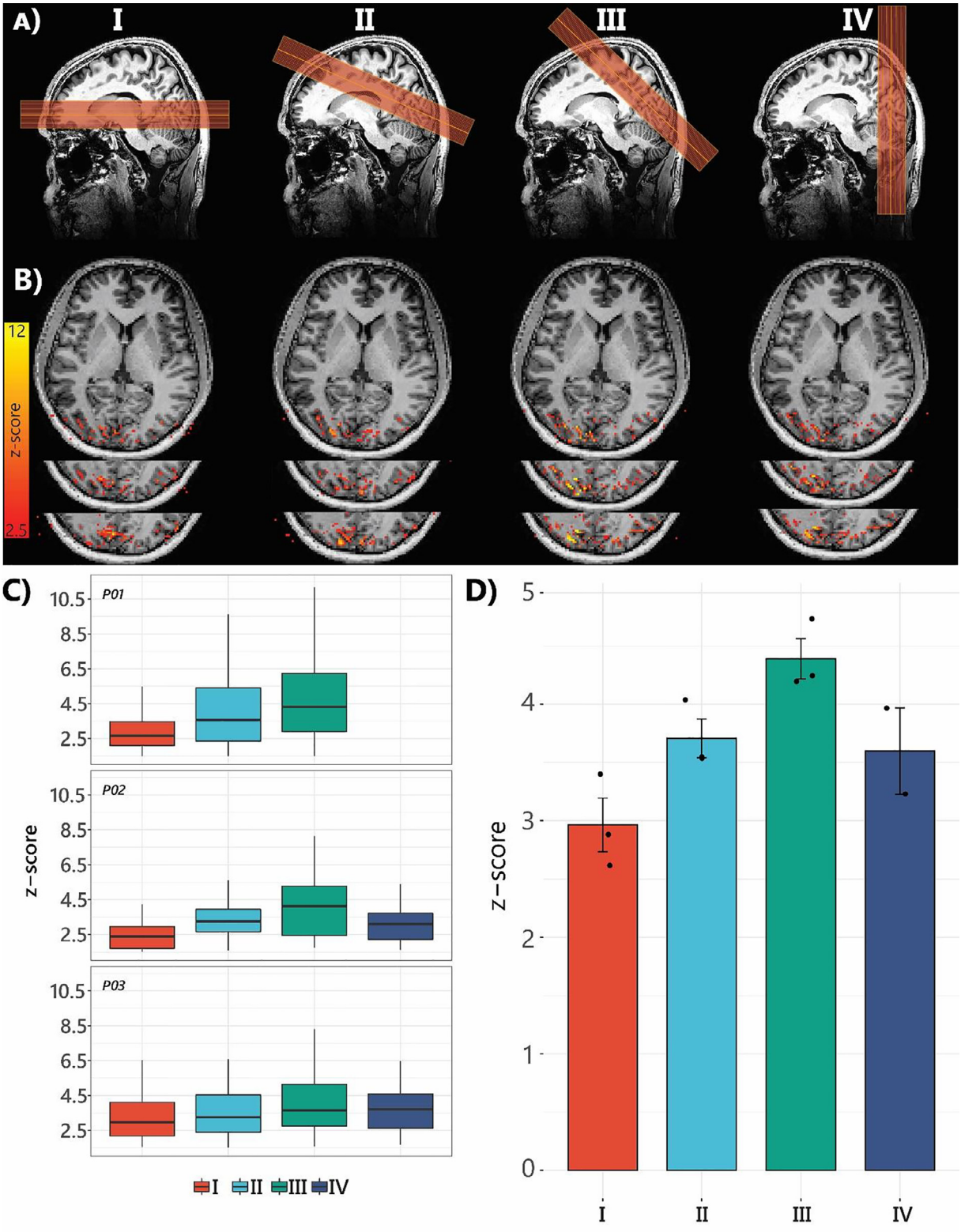

Fig. 1. We evaluated four different slice orientations to find the optimal orientation for visual responses in a VASO–CBV experiment. (A) Four slice orientations: (I) Aligned with the Anterior-Posterior Commissure with the phase encoding in the Anterior-Posterior direction, (II) parallel to the calcarine sulcus with phase encoding in the Anterior-Posterior direction, (III) aligned with the cerebellar superior surface, with phase encoding in the Right-Left direction, and (IV) perpendicular to the calcarine sulcus with phase encoding in the Right-Left direction. In all orientations, the calcarine sulcus was included in the slab. (B) VASO–CBV activated voxels ($z > 2.5$) within the shared volume of all orientations, overlaid on the anatomical data. (C) Boxplot of the Z-scores within the overlap ROI per participant. (D) Z-score averaged across participants (the data points represent each participant). Both in single participants and averaged data, slice orientation (III) yielded the strongest signals.

direction, (III) aligned with the cerebellar superior surface, with phase encoding in the Right-Left direction, and (IV) perpendicular to the calcarine sulcus (coronal orientation) with phase encoding in the Right-Left direction (Fig. 1A). Fig. 1A shows the four slice orientation planes (I–IV). Fig. 1B shows VASO-CBV activated voxels ($z > 2.5$) within the shared volume of all orientations, overlaid on the anatomical data. Robust VASO-CBV responses in the visual cortex were detected in all participants for all orientation planes (Fig. 1B).

We summarized the slice orientation results by computing the average response into Z-scores within the overlap ROI. The results of the slice orientation experiment are shown in Fig. 1C and D, for individual participants and averaged across participants, respectively. The third slice orientation option (III) yielded the highest average Z-scores across individual and group averaged data. The Z score of orientation III was significantly different than the other orientations. The post hoc Holm correction showed differences between I vs III: $p < 0.001$, II vs III: $p = 0.016$, III vs IV: $p = 0.04$. There was also a significant difference between I and IV ($p = 0.04$).

Supplementary Fig. 2A shows an example of tSNR maps for one of the participants (P02) across all four orientations and the group mean across participants. The tSNR values were higher for orientation III, with no statistical significance difference. In addition, we observed insufficient fat suppression in the EPI readout for all three participants, which led to larger ghosting, notably for orientation II (Supplementary Fig. 2B). Supplementary Fig. 2B shows a direct comparison between orientation II and III. We did not observe ghosting artifacts due to insufficient fat suppression for the other orientations. Hence, all subsequent experiments used an orientation of the slab aligned with the superior surface of the cerebellum, covering the calcarine sulcus in a coronal-oblique plane with the phase-encoding direction along the right-left axis.

3.2. VASO-CBV and BOLD population receptive field responses

The variance explained maps show the fMRI signal quality captured by the pRF model (Fig. 2). These responses covered the target visual area (V1–V3) for all three examples, although the 14-run average BOLD shows more robust voxel responses. The single BOLD run shows a lower but still a comparable explained variance. For VASO-CBV, the extension of the variance explained map is similar to the single BOLD run. The example voxel was selected to have a high variance explained ($R^2 = 78.87\%$) in the VASO-CBV responses and was directly compared to the BOLD responses in the same voxel, in a single run, averaged over 14 runs. The VASO-CBV time series exhibits a lower response amplitude than the BOLD time series. The single BOLD run has a comparable signal change to the 14-average BOLD run but has a much higher noise floor, leading to a worse model fit and lower R^2 value. Note that the difference in amplitude for BOLD and VASO-CBV is expected and reflects their sensitivity differences.

The pRF visual field maps are shown in Fig. 3. BOLD pRF maps show the expected pattern of a complete visual field representation (Dumoulin and Wandell, 2008). VASO-CBV maps show a similar pattern for eccentricity and polar angle. The similarity between BOLD and VASO-CBV pRFs was quantified using a Pearson's correlation test on the eccentricity values (Fig. 3F). The correlation was strong and statistically significant for all regions and participants at ($R = 0.83 \pm 0.11$ [Mean ± SD], $p < 0.0001$). Most slope values of the fits were close to the unity line, where eccentricity equates between VASO-CBV and BOLD (> 0.9). Apart from V3 for P04 and P05; and V2 for P05, the measured slope was 0.73, 0.38, and 0.72, respectively. The pRF maps for the other two participants are depicted in Supplementary Fig. 3. These results show that pRF maps can be obtained reliably with VASO-CBV as well as with BOLD.

Fig. 4 shows the tSNR (Panel A) and variance explained (Panel B) as a function of the number of runs for BOLD and VASO-CBV. For both BOLD and VASO-CBV, the tSNR increases with the number of runs for both regions and participants in similar proportions with higher values for BOLD than VASO-CBV. Note that the differences between gray and white matter are most likely caused by the stimulus-driven signal fluctuations in the gray matter, baseline signal intensity, and non-task-related BOLD signal fluctuations, all leading to lower tSNR values in the gray matter relative to the white matter. The variance explained in V1 does not increase at the same rate and amplitude for both acquisitions: For BOLD, the same selected voxels can reach 70% variance explained at a cumulative sum of 14 runs (average), whereas the VASO-CBV explained variance in the same voxels approaches 30%, approximately the same variance explained as a single run of BOLD data.

The comparison of pRF sizes obtained from BOLD and VASO-CBV runs was performed between the 14-run averaged VASO-CBV data and for each BOLD run to maintain similar levels of variance explained. A linear increase of pRF size with eccentricity is expected for all visual field areas, with increasing slopes for more downstream areas (Dumoulin and Wandell, 2008). As expected, the pRF size increases as a function of eccentricity for both BOLD and VASO-CBV (Fig. 5). The slope of this function increases from V1 to V3 in almost all volunteers. The only exception is P05, presenting a nearly similar slope for V2 and V3. However, in contrast to our hypothesis, we did not observe smaller pRF sizes derived from VASO-CBV than BOLD-derived pRF sizes. A one-way Bayesian ANOVA was performed to test the differences between pRF size in BOLD and VASO-CBV. In the Bayesian framework, the alternative hypothesis is the difference in the means between the averaged 14 VASO-CBV and the individual BOLD runs. We defined the alternative hypothesis as the difference between the averaged 14 VASO-CBV and the individual BOLD runs. The Bayesian ANOVA indicated weak evidence for the alternative hypothesis in V1 ($BF_{10} = 2.687$). Moreover, no evidence was found for the alternative hypothesis in V2 ($BF_{10} = 1.044$) and V3 ($BF_{10} = 0.477$). These results indicate that the pRF sizes for BOLD and VASO-CBV are not significantly different.

4. Discussion

4.1. Overview of the results

In the present study, we evaluated the feasibility of VASO-CBV 7T fMRI for pRF mapping. The SS-SI VASO sequence with 3D EPI readout enabled us to simultaneously acquire BOLD and VASO-CBV responses in the visual cortex. Because of the longer arterial arrival time of the visual cortex, we firstly aimed at the slice optimization of the VASO-fMRI sequence. The optimal orientation that yielded a higher activation level (Z-score) was used in the pRF mapping experiment. We found similar pRF positions, i.e. eccentricity and polar angle, for VASO-CBV and BOLD derived maps. Likewise, the pRF size changed with eccentricity in V1-V3 for VASO-CBV and BOLD in a similar manner. Because of its distinct sensitivity to microvascular blood volume changes, we anticipated that VASO–CBV would show smaller pRF sizes than BOLD. However, we found very similar pRF size estimates for BOLD and VASO-CBV. These results suggest that, for the spatial resolution used here, the vascular component of the pRF size is not dominating in either VASO–CBV or BOLD.

4.2. Slice optimization

The way the CBV contrast is generated in VASO-CBV images implies limitations in acquisition parameters. The readout blocks have to be timed so that the blood signal is nulled or close to zero, e.g., a certain time after the inversion pulse. During this time, fast inflowing blood may enter the slab if vessels transport non-inverted blood fast enough to the area of interest. The so-called inflow effects lead to bright signals in small arteries and an unwanted Cerebral Blood Flow (CBF) contribution, resulting in low sensitivity to CBV changes. At the same time, we assume that all blood is replenished before the BOLD weighted image is acquired (~1.5 s after inversion). The manifestation of the inflow effect depends on several experimental conditions, including the transmit

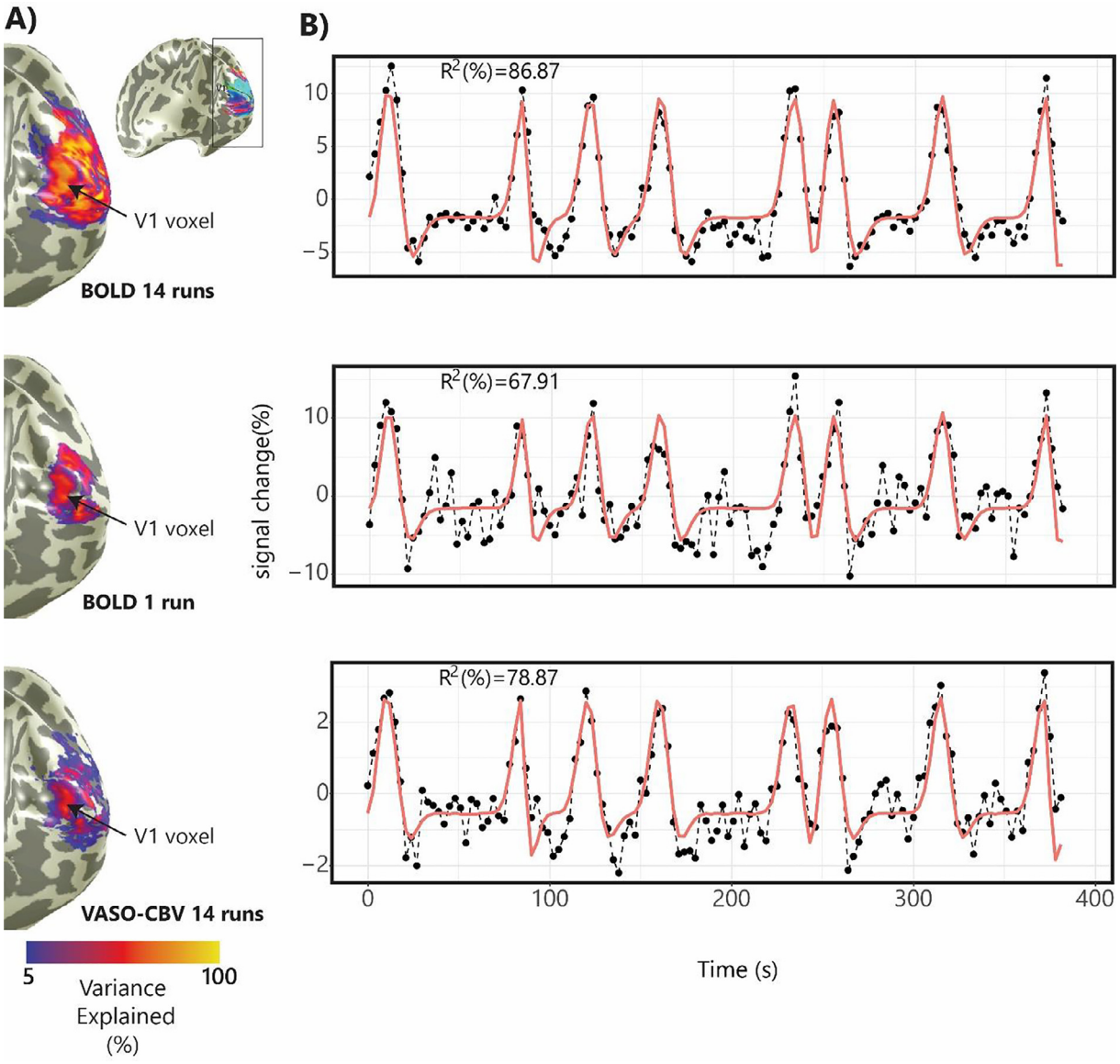

Fig. 2. Example time courses and variance explained maps for VASO–CBV and BOLD. V1 is outlined on top of a polar angle map from a representative participant. (A) Map of the variance explained by the pRF model for 14-run average VASO–CBV and two BOLD examples, one averaged over 14 runs and a single run. (B) An example pRF fMRI responses from a voxel located in V1, for VASO–CBV, averaged over 14 runs and two BOLD examples, one averaged over 14 runs and a single run. The dashed lines with bullet points represent the measured response, and the red line represents the model prediction. R^2 denotes the amount of variance explained by the model for the selected voxel.

coil coverage, inversion time, and functional task. For example, the arterial arrival time is expected to be shorter during the task because of the dilatation of the vessels and the changes in the flow velocity. For the visual cortex, the arterial arrival time is much longer than in the more superior motor cortex (Mildner et al., 2014), potentially affecting blood refilling in an occipital imaging slab.

Here, we positioned the slice orientation to ensure that the slab covered V1–V3 used a short TI to limit inflow effects in VASO-CBV images even during the task, while sufficient refilling occurred to achieve good VASO-CBV sensitivity. The coverage of the transmit coil determines the area of tissue in which a complete inversion of the signal is achieved and does not differ between slice orientations. We did not observe indications of inflow artifacts in any of the orientation planes. Nevertheless, the absence of clearly visible inflow artifacts is not complete evidence of no residual inflow effect in the data (Huber et al., 2018b).

Still, orientation III yielded higher z-scores than the other orientations. One possible cause for this difference was the quality of the fat suppression when compared with orientation II (Supplementary Fig. 2). Although not significant, the tSNR measured in the visual area was also higher for orientation III. The proximity and distribution of the channels in the receive coil could also contribute to this result, as SNR and SENSE unfolding depend heavily on the architecture of the rf-coil (Hendriks et al., 2020). Noteworthy, we believed that these findings might depend on other aspects of the sequence. A different spatial resolution might result in a different optimal slice orientation than found here, especially for small voxel sizes where peripheral nerve stimulation (PNS) limits the maximum gradient strength and slew rate. Note that the gradient strength did not limit our experiment, and the PNS level was low according to the vendor measurements.

4.3. tSNR and variance explained differences

Another challenge for the VASO sequence is the inherent lower SNR. In the present study, VASO-CBV tSNR was consistently lower than BOLD.

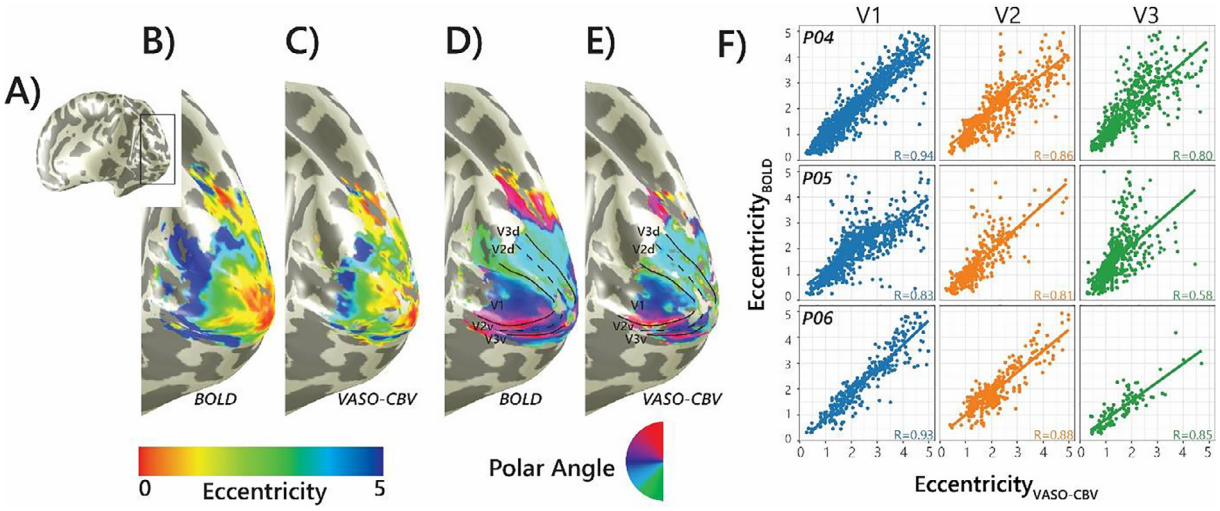

Fig. 3. pRF position estimates on an inflated cortical surface. (A) The visual area (occipital pole) is indicated on the inflated cortical surface. The eccentricity maps are shown for BOLD (B) and VASO-CBV (C). Polar angle maps are likewise compared between BOLD (D) and VASO-CBV (E). Maps are threshold at a variance explained of 5%. (F) Correlations between eccentricity values obtained from BOLD and VASOCBV indicate a similar progression of pRF values across eccentricity between the two sequences. R-value is the Pearson correlation coefficient.

A previous study observed similar behavior using similar spatial resolution and readout strategies in the motor area (Huber et al., 2018a). The tSNR curves in Fig. 4A reveal that, in general, a single BOLD run is equivalent to 4, 5 average runs of VASO-CBV. This low tSNR value limits the detection of VASO fMRI signal activation and increases the experimental time compared to typical BOLD acquisitions. The pRF model performance was measured by the variance explained (R^2). For both VASO-CBV and BOLD, the variance explained increases with the number of runs, although in different ratios, with BOLD reaching a plateau earlier than VASO-CBV. Therefore, we compared the average of 14 runs of VASO-CBV to individual BOLD runs in the pRF size analysis.

A promising approach for further VASO-CBV improvements is using denoising techniques, for example, the recently proposed noise reduction with distribution corrected PCA (NORDIC PCA) (Moeller et al., 2021). NORDIC PCA denoising targets the removal of the thermal noise contribution to fMRI, leading to improvements in temporal SNR, functional signal detection (more significant activated voxels), and accuracy of functional maps (Vizioli et al., 2021). Such a denoising technique could improve VASO-CBV tSNR resulting in reduced acquisition times with fewer runs. Of course, BOLD runs also benefit from denoising, and the need to average higher numbers of runs for VASO-CBV might not change.

4.4. VASO-CBV and BOLD pRF estimations

Polar angle and eccentricity maps derived from BOLD contrast were consistent with previous fMRI findings (Dumoulin and Wandell, 2008). The maps derived from VASO-CBV contrast were similar, but because of the lower tSNR less spatially extensive than BOLD at a given threshold (Supplementary Fig. 3). Our results show that VASO-CBV eccentricity has a strong correlation with BOLD eccentricity (Fig. 3). The pRF tuning width changed with the eccentricity (Fig. 5) in V1–V3 for all three participants, similarly for BOLD and VASO–CBV. The pRF variations observed here correspond to the same pattern as in previous reports (Dekker et al., 2019; Dumoulin and Wandell, 2008; Harvey and Dumoulin, 2011). Interestingly, pRF size measurements for VASO-CBV are not smaller than BOLD. The expected higher microvascular specificity of VASO-CBV does not directly result in smaller pRF size estimates for the present pRF experiment.

The pRF size estimate depends on a combination of two types of signal components; neural and non-neural. For the neural component, the position scatter of the individual receptive fields of the recorded neural population contributes to the overall pRF size (Dumoulin and Wandell, 2008). Since the comparison was performed in the same cortical locations, the position scatter is not expected to differ in VASO-CBV compared to BOLD. The non-neural components have different origins: Previous studies showed that eye movements could cause an increase in the pRF size (Klein et al., 2014; Levin et al., 2010). Similarly, head movement-related motion artifacts add noise to the measured responses and reduce the model prediction accuracy, leading to broader measured pRF sizes. Because VASO-CBV and BOLD signals are collected within the same functional run, movement related artifacts are not likely to differ between VASO-CBV and BOLD. Additionally, the V1–3 pRF size variations (Fig. 5) are similar to previous studies (Dumoulin and Wandell, 2008), which provide further evidence that these methodological aspects did not dominate our results. Last, another factor that may influence the observed pRF size estimate is the SNR (Lerma-Usabiaga et al., 2020). However, the high SNR case of 14-run averaged BOLD shows no difference in observed pRF size of single run pRF estimates (Fig. 5), therefore, we do not think that variations in SNR were a factor of influence.

The hemodynamic response properties may also influence the pRF size measurements (Dumoulin and Wandell, 2008; Klein et al., 2014; Lerma-Usabiaga et al., 2020). To investigate the impact of the HRF, we added an HRF fit procedure in addition to the pRF parameters estimation (Harvey and Dumoulin, 2011). For comparison, we also analyzed the pRF sizes obtained using the canonical HRF. The results with the canonical HRF and fitted HRF are near identical (see Supplementary Fig. 1). Taking these results together, we do not believe that the HRF properties affected the VASO and BOLD pRF size.

Therefore, our results suggest that either (1) the spatial vascular contributions to VASO-CBV and BOLD signals do not differ or (2) that the vascular contributions to the pRF estimates are small. We favor the second explanation. First, there are ample studies suggesting different vascular contributions to the VASO-CBV and BOLD signals (Huber et al., 2017, 2021; Jin and Kim, 2008). Second, the pRF estimates from BOLD fMRI and direct neural recordings are similar in the same subjects, both in humans (Harvey et al., 2013; Hermes et al., 2017) and primates (Klink et al., 2021). Furthermore, these pRF estimates match the spatial location of electrically induced visual sensations further linking pRF measurements with perception (Winawer and Parvizi, 2016). Thus, we suggest that pRF measurements are dominated by neural components

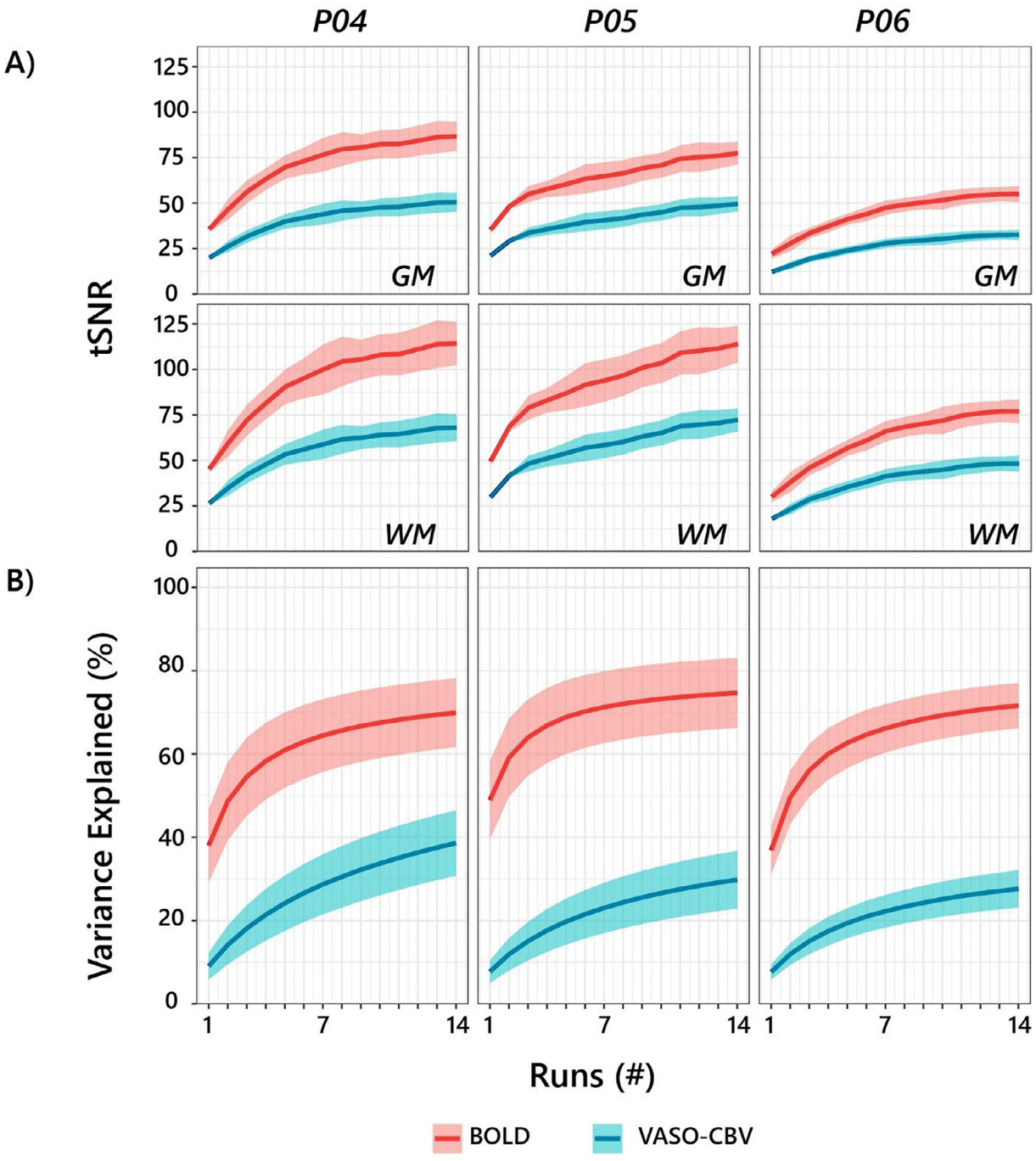

Fig. 4. Quantification of the noise level assessed by tSNR and variance explained as a function of the number of runs. (A) The tSNR increases with the number of averaged runs for all participants and both tissue types in similar proportions. BOLD tSNR is higher than VASO-CBV for all regions and participants. (B) The increase in variance explained is not at the same rate and amplitude for BOLD and VASO-CBV. For BOLD, variance explained plateaus earlier than the VASOCBV variance explained, but the levels of variance explained by BOLD are consistently higher.

and that the vascular contribution to the pRF size measurements are minimal and thus pRF estimates derived from VASO-CBV and BOLD signals will be similar.

These findings are specific for the experimental setup used in the present study, including the spatial resolution used here. Higher spatial resolutions, e.g. 1 mm or lower, may elicit different pRF size estimates, especially if investigated across cortical depth where the VASO-CBV specificity is more pronounced since it is much less sensitive to the draining vein effect than BOLD. Thus, we speculate that in a situation in which both the neural component of the pRF decreases in size and VASO-CBV is less sensitive to the large draining veins, there may be a difference between pRF estimates derived from BOLD and VASO-CBV. However, the VASO-CBV experiments would become practically unfeasible in terms of scan time.

5. Conclusion

In the present study, we investigate how VASO-CBV compares to BOLD fMRI for cognitive neuroscience applications. We compared population receptive field (pRF) mapping estimates between BOLD and VASO-CBV by extending the pRF mapping method to VASO-CBV fMRI at 7T. We simultaneously obtained VASO-CBV and BOLD weighted fMRI

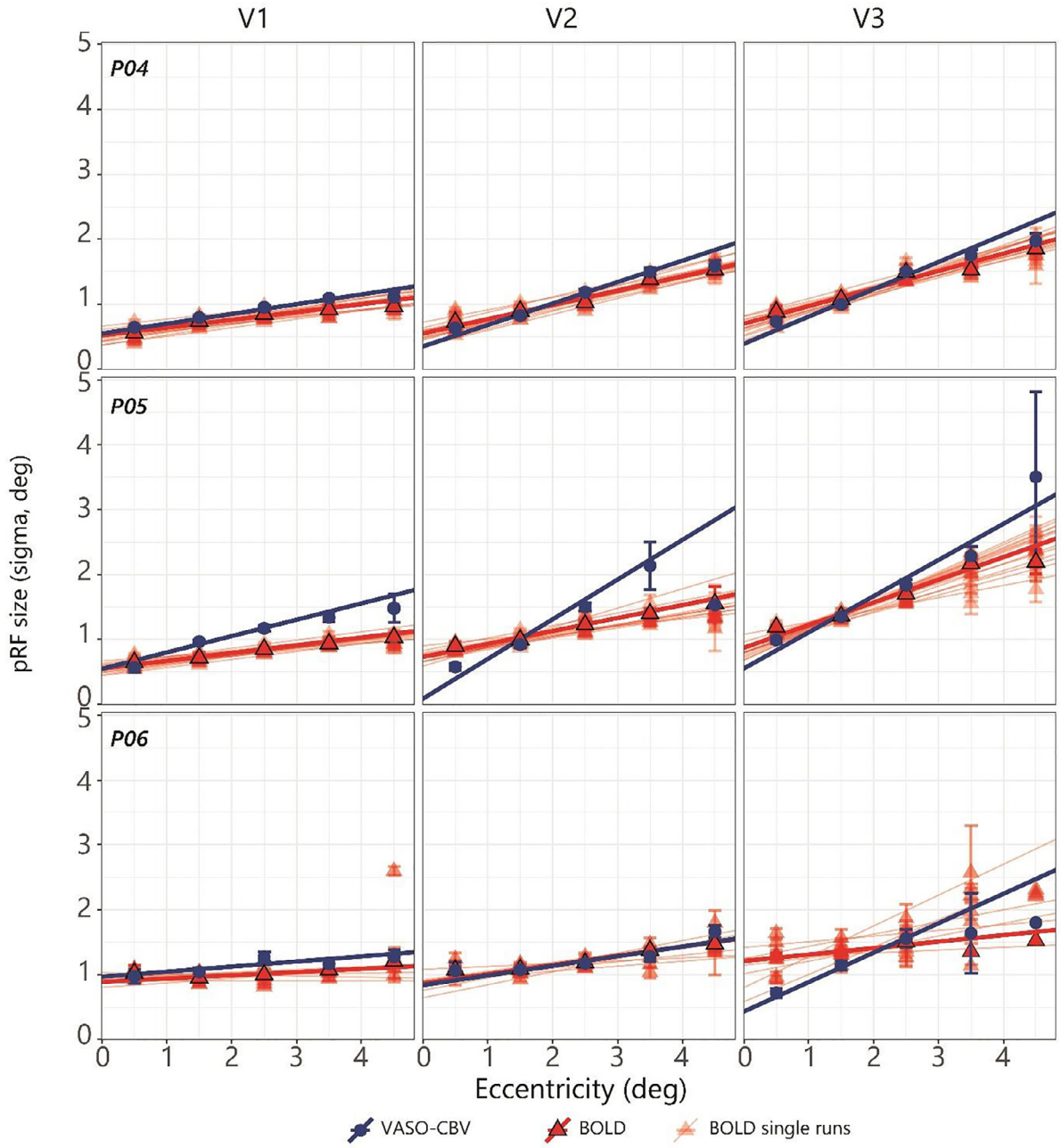

Fig. 5. pRF size changes across eccentricity in V1–V3 for all participants, for the averaged VASO-CBV 14 runs, the averaged BOLD 14 runs, and the individual BOLD runs. pRF sizes increase with visual field eccentricity and across the visual area hierarchy.

using a double readout 3D SS-SI-VASO sequence. The VASO-CBV reliably shows similar polar angle and eccentricity maps to BOLD-based data. The pRF size increased systematically, both with eccentricity and going from V1 to V3, with a high similarity between BOLD and VASO-CBV measured pRF sizes. The expected higher microvascular specificity of VASO-CBV did not directly result in a smaller pRF size. These results suggest that the vascular contribution in the spatial pRF size is minimal or very similar for VASO-CBV and BOLD for the spatial resolution used here.

Data availability

Raw MRI data will be available upon request to the authors. MRI data is considered personal data pursuant to General data protection regulation (GDPR) and can only be shared based on and subject to the Royal Netherlands Academy of Arts and Sciences (KNAW) policies. Considering the requirements imposed by law and the sensitive nature of personal data, any requests will be addressed on a case-by-case basis, subject to a data usage agreement.

Credit authorship contribution statement

Ícaro A.F. Oliveira: Conceptualization, Investigation, Formal analysis, Methodology, Writing – original draft. **Yuxuan Cai:** Conceptualization, Methodology, Writing – review & editing. **Shir Hofstetter:** Conceptualization, Methodology, Writing – review & editing. **Jeroen C.W. Siero:** Supervision, Conceptualization, Writing – review & editing. **Wietske van der Zwaag:** Supervision, Conceptualization, Writing – review & editing. **Serge O. Dumoulin:** Supervision, Conceptualization, Methodology, Writing – review & editing.

Acknowledgements

This work was supported by Royal Netherlands Academy for Arts and Sciences (KNAW) research grant (2018, to S.O.D., W.Z, J.S.), and by the Netherlands Organization for Scientific Research (NWO) Vidi Grant (TTW VI.Vidi.198.016 to W.Z.), Vici (016.Vici.185.050 to S.O.D.), and a China Scholarship Council (CSC) Scholarship [201706750008] (Y.C.).

Supplementary materials

Supplementary material associated with this article can be found, in the online version, at doi:10.1016/j.neuroimage.2021.118868.

References

Aqil, M., Knapen, T., Dumoulin, S.O., 2021. Divisive normalization unifies disparate response signatures throughout the human visual hierarchy. Proc. Natl. Acad. Sci. 118, e2108713118. doi:10.1073/pnas.2108713118.

Bazin, P.L., Weiss, M., Dinse, J., Schäfer, A., Trampel, R., Turner, R., 2014. A computational framework for ultra-high resolution cortical segmentation at 7Tesla. Neuroimage 93, 201–209. doi:10.1016/j.neuroimage.2013.03.077.

Beckett, A.J.S., Dadakova, T., Townsend, J., Huber, L., Park, S., Feinberg, D.A., 2020. Comparison of BOLD and CBV using 3D EPI and 3D GRASE for cortical layer functional MRI at 7 T. Magn. Reson. Med. doi:10.1002/mrm.28347, mrm.28347.

Boynton, G.M., Engel, S.A., Glover, G.H., Heeger, D.J., 1996. Linear systems analysis of functional magnetic resonance imaging in human V1. J. Neurosci. 16, 4207–4221. doi:10.1523/jneurosci.16-13-04207.1996.

Brainard, D.H., 1997. The psychophysics toolbox. Spat. Vis. 10, 433–436. doi:10.1163/156856897X00357.

Buxton, R.B., Griffeth, V.E.M.M., Simon, A.B., Moradi, F., 2014. Variability of the coupling of blood flow and oxygen metabolism responses in the brain: a problem for interpreting BOLD studies but potentially a new window on the underlying neural activity. Front. Neurosci. 8, 1–6. doi:10.3389/fnins.2014.00139.

Cai, Y., Hofstetter, S., Van Der Zwaag, W., Zuiderbaan, W., Dumoulin, S.O., 2021a. Individualized cognitive neuroscience needs 7T: comparing numerosity maps at 3T and 7T MRI. Neuroimage 237, 118184. doi:10.1016/j.neuroimage.2021.118184.

Cai, Y., Hofstetter, S., Van Dijk, J., Zuiderbaan, W., Van Der Zwaag, W., Harvey, B.M., Dumoulin, S.O., 2021b. Topographic numerosity maps cover subitizing and estimation ranges. Nat. Commun. 121 (12), 1–10. doi:10.1038/s41467-021-23785-7, 2021.

Dekker, T.M., Schwarzkopf, D.S., De Haas, B., Nardini, M., Sereno, M.I., 2019. Population receptive field tuning properties of visual cortex during childhood. Dev. Cogn. Neurosci. 37. doi:10.1016/J.DCN.2019.01.001.

Donahue, M., MacIntosh, B., Sideso, E., Bright, M., Kennedy, J., Handa, A., Jezzard, P., 2009. Absolute cerebral blood volume (CBV) quantification without contrast agents using inflow vascular-space-occupancy (iVASO) with dynamic subtraction. In: Proceedings of the 17th Annual Scientific Meeting of the International Society. Honolulu, p. 627.

Dumoulin, S.O., Knapen, T., 2018. How visual cortical organization is altered by ophthalmologic and neurologic disorders. Annu. Rev. Vis. Sci. 4, 357–379. doi:10.1146/annurev-vision-091517-033948.

Dumoulin, S.O., Wandell, B.A., 2008. Population receptive field estimates in human visual cortex. Neuroimage 39, 647–660. doi:10.1016/j.neuroimage.2007.09.034.

Finn, E.S., Huber, L., Jangraw, D.C., Molfese, P.J., Bandettini, P.A., 2019. Layer-dependent activity in human prefrontal cortex during working memory. Nat. Neurosci. 22, 1687–1695. doi:10.1038/s41593-019-0487-z.

Friston, K.J., Josephs, O., Rees, G., Turner, R., 1998. Nonlinear event-related responses in fMRI. Magn. Reson. Med. 39, 41–52. doi:10.1002/mrm.1910390109.

Glover, G.H., 2011. Overview of functional magnetic resonance imaging. Neurosurg. Clin. N. Am. 22, 133–139. doi:10.1016/j.nec.2010.11.001.

Harvey, B.M., Dumoulin, S.O., 2011. The relationship between cortical magnification factor and population receptive field size in human visual cortex: constancies in cortical architecture. J. Neurosci. 31, 13604–13612. doi:10.1523/JNEUROSCI.2572-11.2011.

Harvey, B.M., Klein, B.P., Petridou, N., Dumoulin, S.O., 2013. Topographic representation of numerosity in the human parietal cortex. Science 341, 1123–1126. doi:10.1126/science.1239052, (80-.).

Havlicek, M., Uludağ, K., 2020. A dynamical model of the laminar BOLD response. Neuroimage 204. doi:10.1016/j.neuroimage.2019.116209.

Hendriks, A.D., D'Agata, F., Raimondo, L., Schakel, T., Geerts, L., Luijten, P.R., Klomp, D.W.J., Petridou, N., 2020. Pushing functional MRI spatial and temporal resolution further: high-density receive arrays combined with shot-selective 2D CAIPIRINHA for 3D echo-planar imaging at 7 T. NMR Biomed. 33, 1–13. doi:10.1002/nbm.4281.

Hermes, D., Nguyen, M., Winawer, J., 2017. Neuronal synchrony and the relation between the blood-oxygen-level dependent response and the local field potential. PLOS Biol 15, e2001461. doi:10.1371/journal.pbio.2001461.

Hofstetter, S., Cai, Y., Harvey, B.M., Dumoulin, S.O., 2021. Topographic maps representing haptic numerosity reveals distinct sensory representations in supramodal networks. Nat. Commun. 12, 221. doi:10.1038/s41467-020-20567-5.

Hofstetter, S., Dumoulin, S.O., 2021. Tuned neural responses to haptic numerosity in the putamen. Neuroimage 238, 118178. doi:10.1016/j.neuroimage.2021.118178.

Huber, L.R., Poser, B.A., Kaas, A.L., Fear, E.J., Dresbach, S., Berwick, J., Goebel, R., Turner, R., Kennerley, A.J., 2021. Validating layer-specific VASO across species. Neuroimage 237, 118195. doi:10.1016/j.neuroimage.2021.118195.

Huber, L., Finn, E.S., Chai, Y., Goebel, R., Stirnberg, R., Stöcker, T., Marrett, S., Uludag, K., Kim, S.G., Han, S.H., Bandettini, P.A., Poser, B.A., 2020a. Layer-dependent functional connectivity methods. Prog. Neurobiol., 101835 doi:10.1016/j.pneurobio.2020.101835.

Huber, L., Finn, E.S., Handwerker, D.A., Bönstrup, M., Glen, D.R., Kashyap, S., Ivanov, D., Petridou, N., Marrett, S., Goense, J., Benedikt, A., Bandettini, P.A., Poser, B.A., Bandettini, P.A., 2020b. Sub-millimeter fMRI reveals multiple topographical digit representations that form action maps in human motor cortex. Neuroimage 208. doi:10.1016/j.neuroimage.2019.116463.

Huber, L., Goense, J., Kennerley, A.J., Trampel, R., Guidi, M., Reimer, E., Ivanov, D., Neef, N., Gauthier, C.J., Turner, R., Möller, H.E., 2015. Cortical lamina-dependent blood volume changes in human brain at 7T. Neuroimage 107, 23–33. doi:10.1016/j.neuroimage.2014.11.046.

Huber, L., Handwerker, D.A., Jangraw, D.C., Chen, G., Hall, A., Stüber, C., Gonzalez-Castillo, J., Ivanov, D., Marrett, S., Guidi, M., Goense, J.B.M., Poser, B.A., Bandettini, P.A., 2017. High-resolution CBV-fMRI allows mapping of laminar activity and connectivity of cortical input and output in human M1. Neuron 96, 1–11. doi:10.1016/j.neuron.2017.11.005.

Huber, L., Ivanov, D., Handwerker, D.A., Marrett, S., Guidi, M., Uludağ, K., Bandettini, P.A., Poser, B.A., 2018a. Techniques for blood volume fMRI with VASO: from low-resolution mapping towards sub-millimeter layer-dependent applications. Neuroimage 164, 131–143. doi:10.1016/j.neuroimage.2016.11.039.

Huber, L., Ivanov, D., Krieger, S.N., Streicher, M.N., Mildner, T., Poser, B.A., Möller, H.E., Turner, R., 2014. Slab-selective, BOLD-corrected VASO at 7 tesla provides measures of cerebral blood volume reactivity with high signal-to-noise ratio. Magn. Reson. Med. 72, 137–148. doi:10.1002/mrm.24916.

Huber, L., Tse, D.H.Y., Wiggins, C.J., Uludağ, K., Kashyap, S., Jangraw, D.C., Bandettini, P.A., Poser, B.A., Ivanov, D., 2018b. Ultra-high resolution blood volume fMRI and BOLD fMRI in humans at 9.4 T: capabilities and challenges. Neuroimage 178, 769–779. doi:10.1016/j.neuroimage.2018.06.025.

Hurley, A.C., Al-Radaideh, A., Bai, L., Aickelin, U., Coxon, R., Glover, P., Gowland, P.A., 2010. Tailored RF pulse for magnetization inversion at ultrahigh field. Magn. Reson. Med. 63, 51–58. doi:10.1002/mrm.22167.

JASP Team, 2021. JASP Version (0.14.1) [*Computer software*].

Jin, T., Kim, S.G., 2008. Improved cortical-layer specificity of vascular space occupancy fMRI with slab inversion relative to spin-echo BOLD at 9.4 T. Neuroimage 40, 59–67. doi:10.1016/j.neuroimage.2007.11.045.

Kim, S.G., Ogawa, S., 2012. Biophysical and physiological origins of blood oxygenation level-dependent fMRI signals. J. Cereb. Blood Flow Metab. 32, 1188–1206. doi:10.1038/jcbfm.2012.23.

Klein, B.P., Harvey, B.M., Dumoulin, S.O., 2014. Article attraction of position preference by spatial attention throughout human visual cortex. Neuron 84, 227–237. doi:10.1016/j.neuron.2014.08.047.

Kleiner, M., Brainard, D., Pelli, D., Ingling, A., Murray, R., Broussard, C., 2007. What's new in psychtoolbox-3. Perception 36, 1–16.

Klink, P.C., Chen, X., Vanduffel, W., Roelfsema, P.R., 2021. Population receptive fields in nonhuman primates from whole-brain fMRI and large-scale neurophysiology in visual cortex. eLife 10. doi:10.7554/eLife.67304.

Lerma-Usabiaga, G., Benson, N., Winawer, J., Wandell, B.A., 2020. A validation framework for neuroimaging software: the case of population receptive fields. PLoS Comput. Biol. 16, 1–18. doi:10.1371/journal.pcbi.1007924.

Levin, N., Dumoulin, S.O., Winawer, J., Dougherty, R.F., Wandell, B.A., 2010. Cortical maps and white matter tracts following long period of visual deprivation and retinal image restoration. Neuron 65, 21–31. doi:10.1016/J.NEURON.2009.12.006.

Lu, H., Basso, G., Serences, J.T., Yantis, S., Golay, X., Van Zijl, P.C.M., 2005. Retinotopic mapping in the human visual cortex using vascular space occupancy-dependent functional magnetic resonance imaging. Neuroreport 16, 1635–1640. doi:10.1097/01.wnr.0000181580.18636.ee.

Lu, H., Golay, X., Pekar, J.J., van Zijl, P.C.M.M., 2003. Functional magnetic resonance imaging based on changes in vascular space occupancy. Magn. Reson. Med. 50, 263–274. doi:10.1002/mrm.10519.

Lu, H., Hua, J., van Zijl, P.C.M., 2013. Noninvasive functional imaging of cerebral blood volume with vascular-space-occupancy (VASO) MRI. NMR Biomed. 26, 932–948. doi:10.1002/nbm.2905.

Marques, J.P., Kober, T., Krueger, G., van der Zwaag, W., Van de Moortele, P.F., Gruetter, R., 2010. MP2RAGE, a self bias-field corrected sequence for improved segmentation and T1-mapping at high field. Neuroimage 49, 1271–1281. doi:10.1016/j.neuroimage.2009.10.002.

Menon, R.S., 2002. Postacquisition suppression of large-vessel BOLD signals in high-resolution fMRI. Magn. Reson. Med. 47, 1–9. doi:10.1002/mrm.10041.

Mildner, T., Müller, K., Hetzer, S., Trampel, R., Driesel, W., Möller, H.E., 2014. Mapping of arterial transit time by intravascular signal selection. NMR Biomed. 27, 594–609. doi:10.1002/nbm.3098.

Moeller, S., Pisharady, P.K., Ramanna, S., Lenglet, C., Wu, X., Dowdle, L., Yacoub, E., Uğurbil, K., Akçakaya, M., 2021. NOise reduction with distribution corrected (NORDIC) PCA in dMRI with complex-valued parameter-free locally low-rank processing. Neuroimage 226. doi:10.1016/j.neuroimage.2020.117539.

Ogawa, S., Lee, T.M., Kay, A.R., Tank, D.W., 1990. Brain magnetic resonance imaging with contrast dependent on blood oxygenation. Proc. Natl. Acad. Sci. USA 87, 9868–9872. doi:10.1073/pnas.87.24.9868.

Oliveira, Í.A.F., Roos, T., Dumoulin, S.O., Siero, J.C.W., van der Zwaag, W., 2021a. Can 7T MPRAGE match MP2RAGE for gray-white matter contrast? Neuroimage 240, 118384. doi:10.1016/j.neuroimage.2021.118384.

Oliveira, Í.A.F., van der Zwaag, W., Raimondo, L., Dumoulin, S.O., Siero, J.C.W., 2021b. Comparing hand movement rate dependence of cerebral blood volume and BOLD responses at 7T. Neuroimage 226, 117623. doi:10.1016/j.neuroimage.2020.117623.

Persichetti, A.S., Avery, J.A., Huber, L., Merriam, E.P., Martin, A., 2019. Layer-specific contributions to imagined and executed hand movements in human primary motor cortex. SSRN Electron. J. 1–5. doi:10.2139/ssrn.3482808.

R Core Team, 2020. A Language and Environment for Statistical Computing. R Found. Stat. Comput.

Uludağ, K., Müller-Bierl, B., Uğurbil, K., 2009. An integrative model for neuronal activity-induced signal changes for gradient and spin echo functional imaging. Neuroimage 48, 150–165. doi:10.1016/j.neuroimage.2009.05.051.

Victor, J.D., Purpura, K., Katz, E., Mao, B., 1994. Population encoding of spatial frequency, orientation, and color in macaque V1. J. Neurophysiol. 72, 2151–2166. doi:10.1152/jn.1994.72.5.2151.

Vizioli, L., Moeller, S., Dowdle, L., Akçakaya, M., De Martino, F., Yacoub, E., Uğurbil, K., 2021. Lowering the thermal noise barrier in functional brain mapping with magnetic resonance imaging. Nat. Commun. 12, 5181. doi:10.1038/s41467-021-25431-8.

Wandell, B.A., Winawer, J., 2015. Computational neuroimaging and population receptive fields. Trends Cogn. Sci. 19, 349–357. doi:10.1016/j.tics.2015.03.009.

Winawer, J., Parvizi, J., 2016. Linking electrical stimulation of human primary visual cortex, size of affected cortical area, neuronal responses, and subjective experience. Neuron 92, 1213–1219. doi:10.1016/j.neuron.2016.11.008.

Yu, Y., Huber, L., Yang, J., Jangraw, D.C., Handwerker, D.A., Molfese, P.J., Chen, G., Ejima, Y., Wu, J., Bandettini, P.A., 2019. Layer-specific activation of sensory input and predictive feedback in the human primary somatosensory cortex. Sci. Adv. 5, eaav9053. doi:10.1126/sciadv.aav9053.